Available online at www.sciencedirect.com
ScienceDirect
Trans. Nonferrous Met. Soc. China 35(2025) 1155−1167
Transactions of Nonferrous Metals Society of China
www.tnmsc.cn

High-temperature fracture behavior of Ti−22Al−26Nb with different featured microstructures

Yong-qiang ZHANG, Ke-min XUE, Miao MENG, Si-liang YAN, Ping LI

School of Materials Science and Engineering, Hefei University of Technology, Hefei 230009, China

Received 23 August 2023; accepted 21 June 2024

Abstract: The fracture behavior at high temperatures of the Ti−22Al−26Nb alloy, which features duplex lamellar, bimodal, and Widmanstätten structures, was studied. Samples of the alloy were prepared through compression deformation in the trans-phase region followed by subsequent heat treatment. The results indicate that at 650 °C, the fracture toughness of the Ti−22Al−26Nb alloy is increased by 41.7% compared to that with original microstructures. The content of the *B*2 phase significantly influences the inherent fracture toughness of the material, while the morphology and distribution of the precipitated phases primarily affect the tortuosity of the crack propagation path. Among the microstructural features, the morphology and geometric orientation of the lamellae most significantly impact the crack path; consequently, the Widmanstätten structure exhibits the most tortuous fracture path. Additionally, a predictive model for fracture toughness is developed, which effectively predicts the fracture toughness of Ti−22Al−26Nb alloys with various microstructures at 650 °C.

Key words: Ti_2AlNb-based alloy; featured microstructures; fracture toughness prediction model; fracture mechanics

1 Introduction

Ti−22Al−26Nb-based alloys have garnered considerable attention for their potential as advanced aerospace and high-temperature materials. Compared to conventional commercial titanium alloys, they exhibit high specific strength, excellent oxidation resistance, and good creep resistance, making them particularly suitable for high-temperature applications [1−5]. The application temperature range for Ti−22Al−26Nb-based alloys typically spans from 650 to 800 °C. Furthermore, the concept of damage tolerance is widely accepted in the aerospace industry [6,7]. Fracture toughness is a critical measure within the damage-tolerance design framework, as it directly influences an aircraft's lifespan [8]. However, the inherently low plasticity of Ti−22Al−26Nb-based alloys, a characteristic of typical intermetallic materials, significantly reduces their fracture toughness, thus limiting their industrial applications [9]. Therefore, exploring methods to enhance the fracture toughness of Ti−22Al−26Nb-based alloys at operational temperatures is crucial.

Recent studies have been extensively focused on the fracture behavior of Ti−Al−Nb alloys [10−15]. Common methods to measure fracture toughness include three-point bending and compact tensile tests. YUE et al [16] investigated the fracture toughness of directionally solidified Ti−46Al−5Nb−0.18C−0.3Si alloy using miniature single-edge notched bend (SENB) specimens. Their findings revealed that increasing the orientation angle of the alloy enhanced its fracture toughness and shifted the fracture mode from interlaminar to translaminar. WANG et al [17] assessed the fracture toughness of solidified Ti−(43−48)Al−2Cr−2Nb alloys using the

Corresponding author: Ping LI, Tel/Fax: +86-551-62901368, E-mail: li_ping@hfut.edu.cn
DOI: https://doi.org/10.1016/S1003-6326(24)66740-3

SENB three-point bending test. The results showed that when the laminate orientation was perpendicular to the loading stress, an increase in *B*2 phase content reduced fracture toughness. Conversely, when the laminate orientation was parallel to the loading stress, the *B*2 phase hindered crack propagation, thereby improving fracture toughness. SHI et al [18] utilized compact tensile specimens to examine the fracture toughness of Ti−5Al−5Mo−5V−1Cr−1Fe titanium alloy with a basket-weave structure and developed a predictive model. They found that a tortuous crack path significantly increased the fracture toughness of the material.

The fracture behavior of Ti−Al−Nb alloys has been thoroughly examined in prior research. FAN et al [19] and ZHENG et al [20] observed that the fracture mechanism of Ti−22Al−25Nb alloy transitions from quasi-cleavage at room temperature to ductile fracture at high temperatures. They noted that a lower volume fraction of the *O* phase and thicker lath *O* phase within the alloy improved fracture toughness by hindering crack propagation. These findings provide valuable insights into the fracture mechanism of Ti−Al−Nb alloys. In addition to experimental studies, crystal plasticity and molecular dynamics simulations have been employed to further explore fracture behavior. FU et al [11] used crystal plasticity simulations to analyze how the size and distribution of the *O* phase affect the fracture properties of Ti2AlNb superalloys, discovering that plastic deformation in the *B*2 phase matrix reduces stress concentration at the *O*/*B* phase interfaces, which in turn prevents microcrack initiation and growth. LIU et al [21] applied molecular dynamics simulations to study how the orientation of the *B*2 phase affects crack propagation in Ti2AlNb-based alloys, finding that crack propagation mechanisms within the *B*2 phase are orientation-dependent. They also noted that defects and stress concentrations at the crack tip facilitate martensitic nucleation, leading to HCP phase formation and increased toughness at the crack tip. Despite these findings, there is still a need for quantitative analysis of fracture toughness in Ti2AlNb-based alloys, taking into account of the complex interplay among microstructure morphology, phase composition, and crack propagation path. Moreover, understanding the intrinsic material properties and their influence on fracture toughness under varying thermodynamic conditions is crucial. To address these issues, our research aims to examine the fracture behavior of Ti2AlNb-based alloys under complex thermo-dynamic paths and provide a quantitative analysis of the effects of material intrinsic properties and crack propagation path on fracture toughness. This research contributes to the enhancement of fracture resistance in Ti−Al−Nb alloys. Therefore, the Ti−22Al−26Nb alloy subjected to thermal compression treatment at different temperatures was selected as the research subject, with various microstructures achieved by adjusting the thermal-deformation parameters.

2 Experimental

To investigate the effects of hot compression processing parameters on the microstructural evolution and fracture toughness of Ti−22Al−26Nb alloys, the following experiments were carried out. Cylindrical bars of the Ti−22Al−26Nb alloy, each measuring 15 mm in diameter and 30 mm in height, were prepared using a wire electric discharge machine (WEDM). Isothermal compression tests were conducted on a Gleeble−3500 testing machine at a compression rate of 0.01 s^{-1} and at target temperatures ranging from 980 to 1060 °C. The height reduction was maintained between 40% and 60%. Following deformation, the samples were subjected to solution treatment at 960 °C for 1 h, followed by water quenching, aging at 780 °C for 12 h, and then air cooling to room temperature. To prevent high-temperature oxidation, a glass lubricant was uniformly applied to the surfaces of the samples before the heat treatment. The process parameters of hot compression and heat treatment of Ti−22Al−26Nb alloy are given in Table 1.

The fracture toughness assessments were conducted using single-edge notched bend (SENB) specimens. Each specimen measured 2.5 mm × 5 mm × 22 mm, as illustrated in Fig. 1. A 0.3 mm notch was created on the side of each specimen using wire electric discharge machining (WEDM), and a fatigue crack was prefabricated using an INSTRON 8871 hydraulic fatigue testing machine. The span for the SENB specimen was set at 20 mm. Test parameters included a stress ratio of 0.1, a frequency of 10 Hz, and a stress intensity factor range (ΔK) of 10.5 MPa·$m^{1/2}$. The initial length of

Table 1 Process parameters of hot compression and heat treatment of Ti−22Al−26Nb alloy

Sample	Deformation parameter	Heat treatment parameter	Target microstructure
S0	–	–	–
S1	980 °C, 50%	(960 °C, 1 h)+ (780 °C, 12 h)	Duplex lamellar
S2	1020 °C, 50%	(960 °C, 1 h)+ (780 °C, 12 h)	Widmanstätten
S3	1060 °C, 50%	(960 °C, 1 h)+ (780 °C, 12 h)	Basketweave
S4	1020 °C, 40%	(960 °C, 1 h)+ (780 °C, 12 h)	Bimodal
S5	1020 °C, 60%	(960 °C, 1 h)+ (780 °C, 12 h)	Lamellar structure

the fatigue crack was measured with an extensometer. Two specimens per hot deformation parameter were tested, and similarly, two specimens for each parameter were used in three-point bending tests. The three-point bending tests were performed on an MTSC44.104 microcomputer-controlled electronic universal testing machine at 650 °C, with a crosshead speed of 0.1 mm/min. The fracture load (P_Q) was recorded directly from the load−displacement curve, and fracture toughness (K_{IC}) for the bending fracture specimen was calculated using the following equation:

$$K_{IC}=\left[\left(\frac{S}{W}\right)\frac{P_Q}{\left(B^2W\right)^{0.5}}\right]\left[g\left(\frac{a}{W}\right)\right] \tag{1}$$

$$g\left(\frac{a}{W}\right)=\left\{\left(2+\frac{a}{W}\right)\left[1.99-\left(\frac{a}{W}\right)\left(1-\frac{a}{W}\right)\cdot\left(2.15-\frac{3.93a}{W}+\frac{2.7a^2}{W^2}\right)\right]\right\}/\left\{2\left(1+\frac{2a}{W}\right)\left(1-\frac{a}{W}\right)^{1.5}\right\} \tag{2}$$

where W is the width of the specimen, B is the thickness, a is the length of the pre-splitting crack including the gap, and S is the span of the load (S=4W). P_Q, the load, was determined at the 95% slope of the linear elastic portion of the load-displacement curve. Fracture toughness was calculated based on the average value from two specimens.

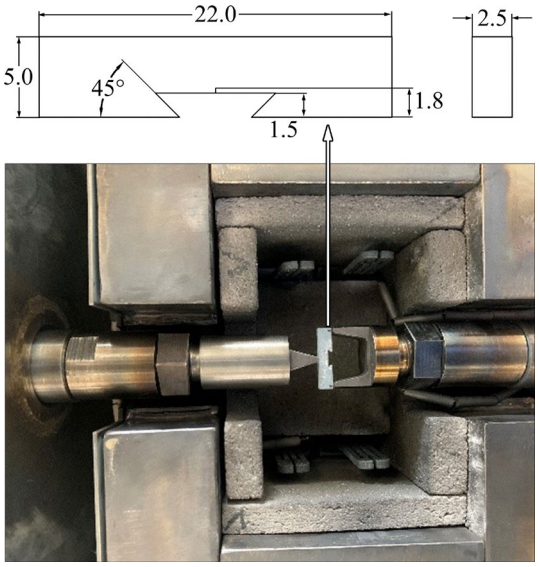

Fig. 1 Schematic diagram of experimental assembly (Unit: mm)

The microstructure, fractography, and fracture path of the specimens were analyzed using a scanning electron microscope (SEM, ZEISS Sigma 300). Quantitative analysis of the microstructure was performed using Image-Pro Plus 6.0 software.

3 Results and discussion

3.1 Microstructure

Figure 2 illustrates the phase composition of the sample as revealed by scanning electron microscopy (SEM). Figure 2(a) shows numerous needle-like *O* phases randomly distributed within the *B*2 phase matrix. Additionally, a small amount of equiaxed *α*2 phase is uniformly distributed within the *B*2 matrix, with the rim-*O* phase encircling the equiaxed *α*2 phase.

Figure 2(b) displays both black equiaxed *α*2 phases and gray *O* phases embedded within the white *B*2 phase matrix. Notably, the *O* phase appears in two distinct sizes, coarse and fine acicular types, creating a characteristic bimodal structure. No pronounced preferential orientation of the *O*-phase laths within this structure is observed. Additionally, a small proportion of the equiaxed *α*2 phase has transformed into the *O* phase.

In Fig. 2(c), numerous lath *O* phases and a few acicular *O* phases are evenly distributed throughout the *B*2 phase matrix, with sparse thick grain boundary *α*2 phase particles. The lath *O* phases within the microstructure display a distinct

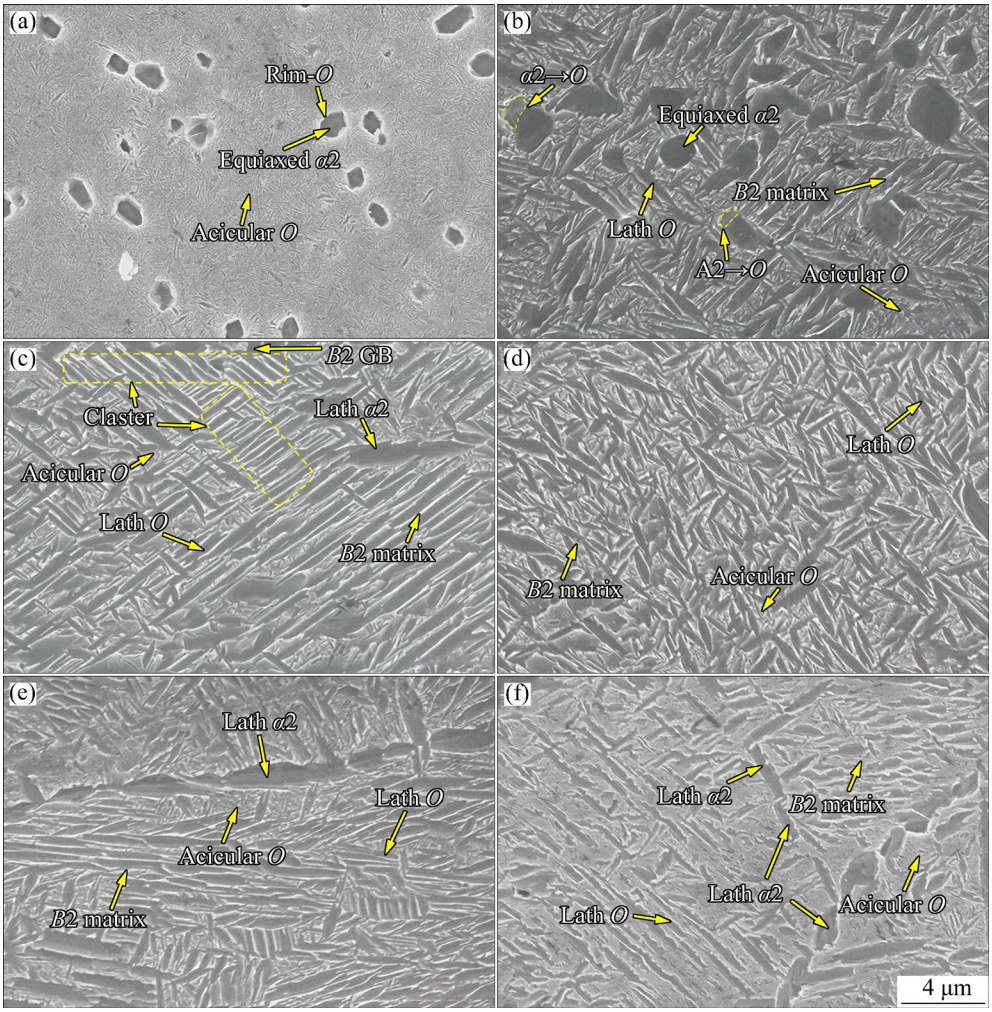

Fig. 2 SEM images of samples with different microstructures: (a) S0; (b) S1; (c) S2; (d) S3; (e) S4; (f) S5

preferential orientation, with most arranging parallel, indicative of a clustered structure.

Figure 2(d) reveals a mixture of both short and thick *O*-phase laths and fine acicular *O* phases within the *B*2 phase matrix. Unlike Fig. 2(c), the lath *O* phases in Fig. 2(d) lack a pronounced preferential orientation and are randomly dispersed within the *B*2 matrix. Sample S3 exhibits characteristics of a basket-weave structure, with laths that are notably shorter and thicker due to multiple nucleation sites and growth impeded by interactions with surrounding solute atoms. The statistical results presented in Table 2 corroborate these observations.

The microstructure in Fig. 2(e) resembles that in Fig. 2(c), showcasing lath *O* phases with preferential orientation, fine needle-like *O* phases, and a minor presence of a cluster-dominant structure.

Figure 2(f) shows the lath *O* phase along with a small amount of acicular *O* phase distributed within the *B*2 phase matrix. The primary difference from the previous structures is the jagged interfaces of the *O* laths, indicating that these are primary *O* laths existing prior to deformation. This observation suggests that during heating, some of the lath *O* phase is retained, and coarsening occurs due to the short holding time. When subjected to 60% height reduction, the *O*-phase lath undergoes deformation from stress and strain, resulting in the formation of serrated defects at its interface with the *B*2-phase matrix. Additionally, the coarse lath *α*2 phase precipitating from the grain boundary undergoes separation and spheroidization under high pressure.

Table 2 presents quantitative data on the microstructural characteristics of Samples S0−S5, detailing the volume fraction of the *B*2-phase matrix and the size characteristics of the lath *O*

phase. Notably, the width of the *O* phase reaches 0.35 μm, categorizing it as a lath *O* phase. The volume fraction of the *B*2 phase in the initial sample, S0, is 36.3%, compared to 51.6% in Sample S5. It is observed that the *B*2 phase content in Samples S1−S4 decreases after deformation and heat treatment, while in Sample S5, it increases, which is an anomaly primarily attributed to significant deformation. The proportion of lath *O* phase in the initial sample is minimal, with a predominance of fine acicular *O* phase, making the influence of the lath *O* phase in Sample S0 negligible. Additionally, the aspect ratio (R_{lath}) of the lath *O* phase in Sample S3 is recorded at 2.94, indicating that it is the shortest and thickest among the samples.

3.2 Fracture morphology

The fracture mechanism can be elucidated by examining the micromorphology of the fracture surfaces. Figure 3 displays the microscopic morphology of fractures in various specimens following a high-temperature three-point bending test. It can be seen that numerous dimples are evident on the fracture surfaces of all samples, indicating rapid and unstable ductile fracture behavior at 650 °C [19]. However, a closer examination of the images reveals significant differences in the size and depth of dimples across different samples. The dimple depths in Figs. 3(a, b) are significantly shallower than those in Fig. 3(c), which, in turn, are shallower than those in Figs. 3(d, e). Additionally, the diameters of the dimples in Figs. 3(a−c) are markedly smaller than those in Figs. 3(d, e), suggesting that the toughness values of Samples S3 and S5 are higher than those of Samples S0−S2. Simultaneously, more uniform cleavage surfaces and a limited number of cleavage steps are observable in Fig. 3(a), typically characterizing a complex quasi-cleavage fracture mechanism [20−22].

A limited number of cleavage planes and steps

Table 2 Average values of main parameters of samples with different microstructures

Sample	K_{IC}/(MPa·m$^{1/2}$)	V_{B2}/% (ε/%)	L_{lath}/μm (ε/%)	W_{lath}/μm (ε/%)	R_{lath} (=L_{lath}/W_{lath})
S0	55.1	36.3 (6.5)	–	–	–
S1	61.9	29.1 (8.2)	2.12 (8.3)	0.51 (12.1)	4.16
S2	62.2	22.6 (9.1)	2.32 (4.9)	0.60 (9.2)	3.86
S3	68.4	34.5 (5.3)	1.56 (6.6)	0.53 (8.5)	2.94
S4	–	30.6 (6.1)	1.98 (9.3)	0.45 (10.5)	4.40
S5	78.0	51.6 (10.1)	1.87 (11.0)	0.43 (6.5)	4.35

K_{IC} is the fracture toughness; V_{B2}, L_{lath}, and W_{lath} are respectively the volume fraction of lamellar *O*, length and width; R_{lath} is the aspect ratio of lath *O* phase; ε is the average relative error

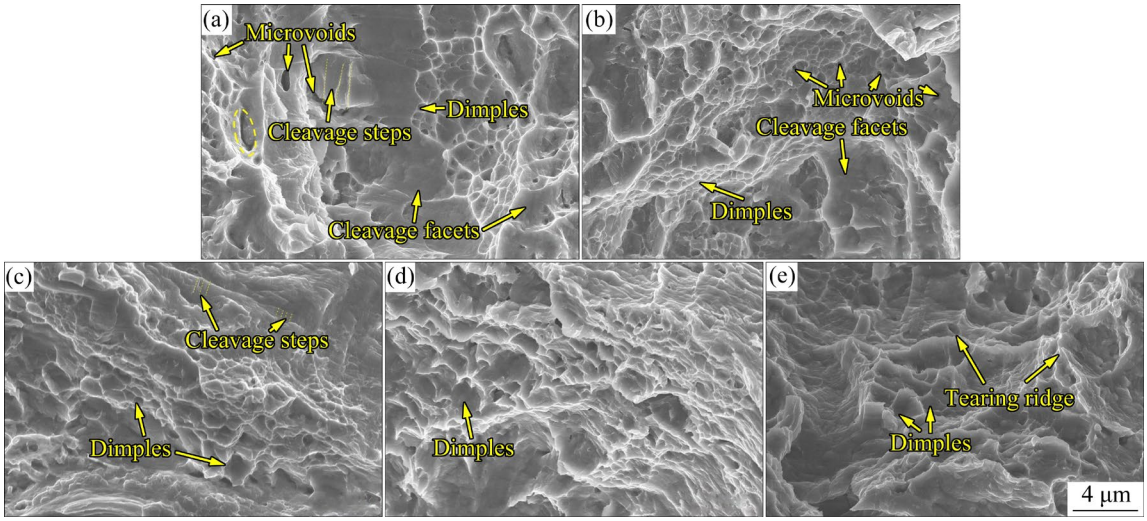

Fig. 3 Microscopic fracture morphologies of different samples at 650 °C: (a) S0; (b) S1; (c) S2; (d) S3; (e) S5

are presented in Figs. 3(b, c), indicating the presence of a fracture mechanism. Compared with Sample S0, the proportion of dimples in Samples S1 and S2 is considerably greater than that of the cleavage planes and steps, suggesting a prevalent ductile fracture mechanism. However, compared to Samples S1 and S2, Sample S0 features a greater number of cleavage surfaces; therefore, the fracture mechanism in Sample S0 is indicative of a quasi-cleavage fracture. Notably, numerous micro-voids exist in Samples S0 and S1, and the proximate voids coalesce, resulting in new elongated cavitations or microcracks.

In conjunction with the microstructure observations in Figs. 2(a, f), it is clear that there is a higher occurrence of equiaxed α2 phases in the microstructures of Samples S0 and S1. Microvoids are formed as the main crack propagates along the interface of the α2 phase, which stimulates the nucleation of microcracks upon encountering the more rigid equiaxed α2 phase during propagation. These newly formed microcracks evolve into holes during further deformation. According to PARADKAR et al [23], the formation, propagation, and accumulation of voids contribute to the acceleration of crack propagation. Numerous dimples characterize Samples S3 and S5, which are larger in diameter and depth than those in Samples S0−S2. Samples S3 and S5 exhibit clear characteristics of ductile fracture. Additionally, prominent white-tearing ridges are observed in Sample S5. Considering the statistical findings regarding *B*2 phase content in Table 2, it is evident that the *B*2 phase content in Sample S5 exceeds that of the other samples, which accounts for the pronounced white-tearing ridges observed in Fig. 3(e). The presence of tearing ridges is a significant indicator of ductile fracture and further suggests that the toughness of Sample S5 surpasses that of Sample S3, consistent with the fracture toughness results presented in Table 2.

3.3 Fracture propagation path

To better understand the fracture mechanisms in various samples at elevated temperatures, it is crucial to observe the crack propagation paths and fracture morphology at characteristic locations. Figure 4 illustrates the characteristic crack propagation paths associated with different initial microstructures, with the dotted arrow indicating the direction of crack propagation.

Figure 4(a) shows the crack propagation path at a characteristic location in Sample S1. Observation reveals that the equiaxed α2 phase can locally alter the crack propagation path to some extent. As shown in Fig. 4(b), a crack propagation direction parallel to the longitudinal axis of the *O* phase laths results in an interlaminar fracture mechanism. A nearly perpendicular angle between the crack propagation direction and the longitudinal axis of the *O* phase lath leads to a translaminar fracture mechanism. Notably, during translaminar fracture, the crack propagation direction shifts by 90°, creating a step-like crack path. An acute angle between the crack propagation direction and the longitudinal axis of the *O* phase lath merges translaminar and interlaminar fracture mechanisms, resulting in a zigzag fracture path.

Figure 4(c) reveals that the crack advances in the form of a crack bridge capable of absorbing significant energy, thus contributing to a toughening effect [16]. The formation mechanism of the crack bridge involves a small angle between the propagation direction of the crack and the longitudinal orientation of *O*-phase lath, where the coordinated response of the matrix *B*2 phase during plastic deformation causes concurrent cracking on both sides of the *O* phase lath. The microstructural analysis indicates that the lath structure in Sample S2 possesses a pronounced preferred orientation, resulting in numerous parallel lath *O* phases.

Figure 4(d) illustrates the crack propagation path in Sample S3, showing that the crack progresses both within and along the grain boundary of the *B*2 phase. As the crack approaches a grain boundary within the interior of the grain, its path may deviate along the grain boundary. This phenomenon becomes particularly pronounced when the α2 phase is present at the grain boundary. As the crack moves along the grain boundary of *B*2 phase, its path is deflected at larger angles due to the tortuosity of the grain boundary. It has been demonstrated that the presence of grain boundaries can extend the crack propagation path, thereby imparting a toughening effect on the material. According to SHAO et al [24], cracks predominantly propagate in areas with low grain boundary density. In regions with high grain boundary density, cracks typically advance along the grain, impeded by the boundary, explaining the aforementioned phenomenon.

Figure 4(e) depicts the characteristic location of the crack propagation path in Sample S5. Observations indicate that as the crack approaches the grain-boundary $\alpha 2$ phase with a coarse lamellar structure, its direction is deflected by nearly 90°. This deflection occurs as the lath $\alpha 2$ phase at the grain boundary impedes crack propagation. Additionally, fine secondary cracks are observed at the locations of the $\alpha 2$ phase lath and the crack tip. SHAO et al [24] demonstrate that $\alpha 2$ phase particles exert a significant blocking effect on the slip of the $B2$ phase, with a strengthening effect surpassing that of the $B2$ grain boundary. Generally, the $\alpha 2$ phase resists plastic deformation. Consequently, crack initiation is facilitated, promoting propagation along the $\alpha 2$ lath/$B2$ matrix phase boundary and altering the propagation direction of crack.

Figure 5 provides a schematic representation

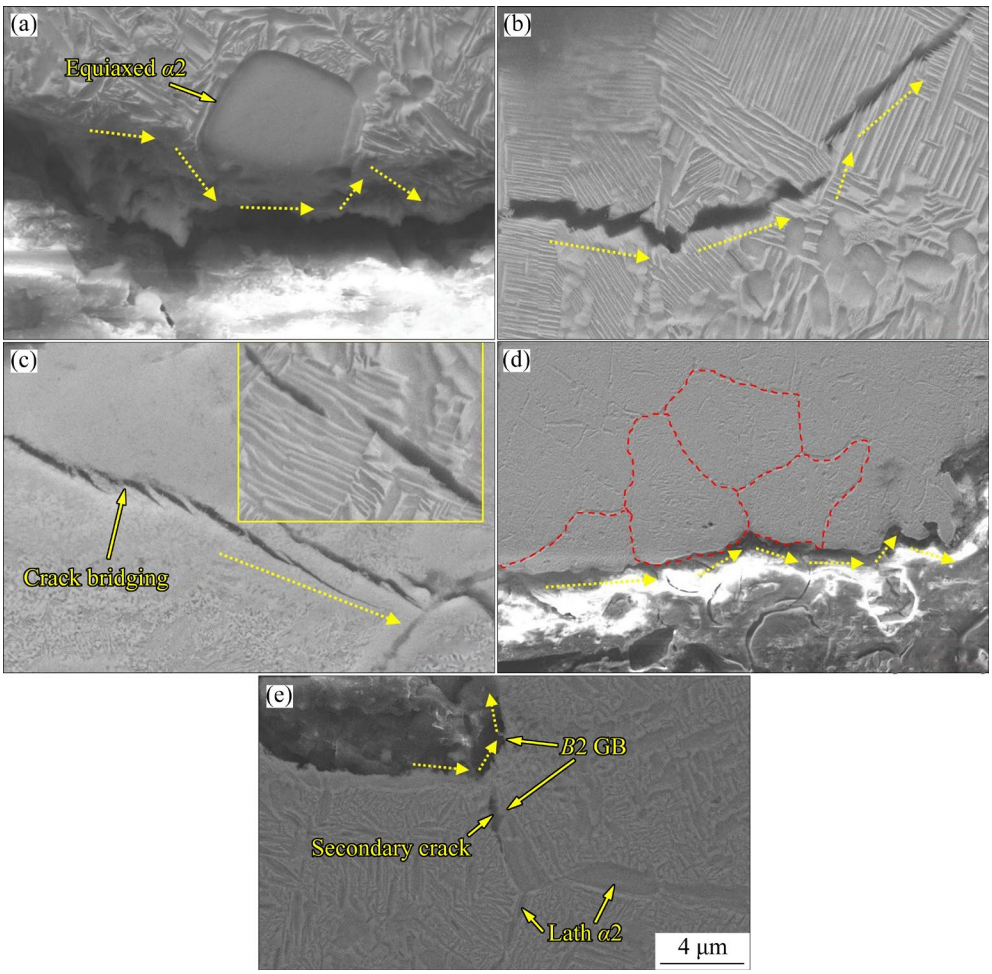

Fig. 4 Characteristic locations in crack propagation paths of different samples: (a) S0; (b) S1; (c) S2; (d) S3; (e) S5

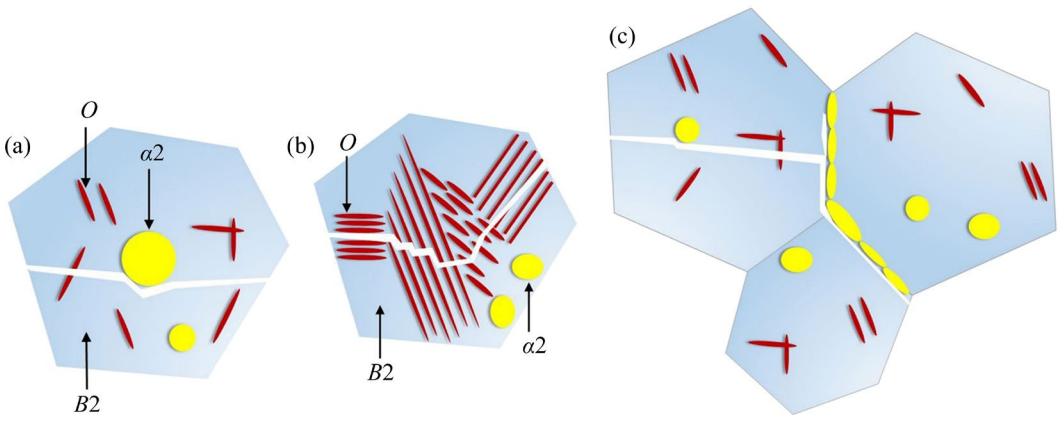

Fig. 5 Crack propagation mechanism of samples with different microstructures

of how various precipitates influence the growth of the primary crack. In Fig. 5(a), the primary crack is shown to circumvent the equiaxed $\alpha 2$ phase. Figure 5(b) demonstrates how different angles between the lath structure and the primary crack result in diverse pathways for the crack passing through the lath *O* phase. The presence of a cluster domain changes the direction of crack propagation, making the pathway more tortuous. Figure 5(c) reveals that the $\alpha 2$ phase, which precipitates at the grain boundary of the *B*2 phase, poses the most significant obstacle to the propagation of the primary crack. Concurrently, these areas also act as nucleation sites for microcracks. Due to the disparate deformation behaviors of the harder $\alpha 2$ and softer *B*2 phase matrices, microcracks emerge at the interface between these two phases.

3.4 Internal and external contribution of fracture properties

The analysis of crack propagation tortuosity was conducted based on the observed crack paths. Generally, crack propagation tortuosity is represented by the following equation:

$$R=\frac{L_{\text{path}}}{L_0} \tag{3}$$

where R denotes the crack propagation tortuosity, L_{path} corresponds to the actual length of the crack path, and L_0 is the projected length of the crack path, as depicted in Fig. 6. Both L_{path} and L_0 were quantitatively analyzed using Image-Pro Plus 6.0. Due to machining errors in the initial crack length measurement, L_0 values across all samples exhibit inconsistency. A higher R value indicates a more tortuous crack path, which contributes externally to fracture toughness.

Specific R-values are detailed in Table 3. Samples S0 and S1 display the lowest R-values, at 1.27 and 1.21, respectively. Observations from Figs. 6(a, b) reveal that the crack expansion paths for Samples S0 and S1 are comparatively straight. Conversely, Sample S2 exhibits the highest R-value of 1.74, indicating the most tortuous expansion path, as shown in Fig. 6(c). Microstructural analysis and observations at characteristic locations suggest that clustered microstructures significantly influence the crack path tortuosity. Notably, a multitude of

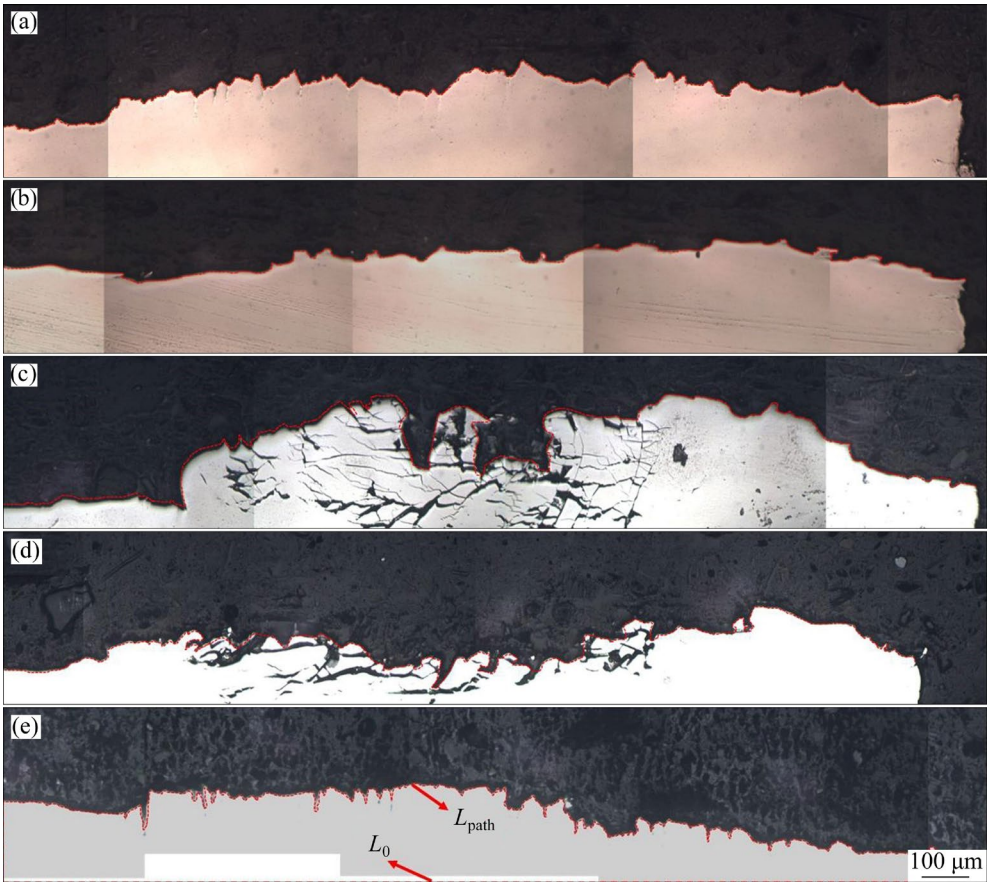

Fig. 6 Crack propagation paths of different samples: (a) S0; (b) S1; (c) S2; (d) S3; (e) S5

Table 3 Quantitative statistics of tortuous degree of crack paths

Sample	L_0/μm	L_{path}/μm	R (=L_{path}/L_0)
S0	1898.5	2413.3	1.27
S1	1593.2	1928.7	1.21
S2	1579.3	2728.3	1.74
S3	1595.7	2392.3	1.44
S5	1557.3	2370.3	1.52

secondary cracks are observed near the primary crack in Sample S2. Furthermore, Fig. 2(c) shows that Sample S2 contains a substantial quantity of parallel plate-like *O* phases. Combined with observations from Fig. 4(c), it is evident that the parallel plate-like *O*-phase structure tends to promote crack bridging, resulting in numerous secondary cracks. Additionally, the *R*-values for Samples S3 and S5 are closely matched, recorded at 1.44 and 1.52, respectively. Based on structural analysis, Sample S3 is characterized by a basket-weave structure with interspersed short lath *O* phases, which contributes to the tortuosity of the crack propagation path. In Sample S5, an increased number of lath $\alpha 2$ phases precipitate at the grain boundary, leading to an alteration in the direction of crack propagation and manifesting as a zigzag crack path.

3.5 Prediction model

Based on previous discussion, ductility and crack path tortuosity represent the intrinsic and extrinsic contributions to fracture toughness, respectively. Consequently, we aim to develop a fracture toughness model that accounts for both intrinsic and extrinsic factors.

Fracture toughness is a critical parameter for evaluating a material's resistance to crack propagation. The value of K_{IC} is largely unaffected by the sample's geometry or the method and mode of loading; it is determined by the critical energy release rate (G_{IC}) during unstable crack propagation under plane strain conditions. According to linear elastic fracture mechanics, the relationship between plane strain fracture toughness (K_{IC}) and critical energy release rate (G_{IC}) is described by the following equation [25]:

$$K_{IC}=\sqrt{\frac{G_{IC}E}{1-\upsilon^2}} \tag{4}$$

where E represents Young's modulus, and υ denotes Poisson's ratio.

As per the Griffith−Orowan−Irwin relation, G_{IC} is given as [26]

$$G_{IC}=2\gamma_{eff} \tag{5}$$

$$\gamma_{eff}=\gamma_p+\gamma_s \tag{6}$$

where γ_s is the surface energy per unit area required for unstable crack propagation at the crack tip, γ_p is the energy absorbed in the plastic deformation of the crack surfaces, and γ_{eff} represents the effective surface energy.

ANTONOV [25] established the correlation between the specific energy of deformation (A_v) and the effective surface energy (γ_{eff}) using the following equation:

$$2\gamma_{eff}\cdot F=A_v\cdot V \tag{7}$$

where V is the volume responsible for failure, and F is the area of the crack forming.

It is important to note that the shape of the plastic zone at the crack tip is traditionally complex, making the calculation of volume (V) and area (F) values challenging [27]. Therefore, this work utilizes the simplified crack-tip plastic zone model proposed by ZHANG et al [28]. Consequently, the failure volume (V) and the crack surface area (F) at the crack tip are obtained as follows:

$$V=\frac{\pi lh}{4}\mathrm{d}b \tag{8}$$

$$F=h\cdot\mathrm{d}b \tag{9}$$

where l, h and db correspond to the major axis length, minor axis length, and thickness of the elliptical zone, respectively. The value of l can be calculated using the empirical engineering equation: $l=0.25(K_{IC}/\mathrm{UTS})^2$ [29]. The average value of l for the present microstructures is 1.47×10^{-3} m.

Then, by introducing Eqs. (8) and (9) into Eqs. (5) and (7), G_{IC} can be expressed as follows:

$$G_{IC}=\frac{\pi l}{4}A_v \tag{10}$$

where the specific energy of deformation (A_v) can be replaced with the deformation work at the uniform deformation stage during the tensile process. A_v can be given as

$$A_v=\int_0^{\varepsilon_u}\sigma\mathrm{d}\varepsilon \tag{11}$$

Subsequently, incorporating Eqs. (9) and (10)

into Eq. (3) defines K_{IC} as follows:

$$K_{IC}=\sqrt{\frac{\pi lE\int_0^{\varepsilon_u}\sigma d\varepsilon}{4(1-\upsilon^2)}} \tag{12}$$

As indicated by Eq. (12), the value of K_{IC} is solely dependent on the material's intrinsic properties. The necessary mechanical parameters can be derived from standard tensile tests to predict the material's intrinsic fracture toughness. However, fracture toughness frequently relies not only on the material's inherent properties but also on the tortuosity of the crack propagation path [30−32]. Several studies have demonstrated that the external contribution to fracture toughness at elevated temperatures significantly exceeds that at room temperature. Therefore, in this study, the tortuosity of the cracks is considered. The tortuosity, R, of the crack is quantitatively expressed as previously mentioned. By introducing R into Eq. (12), the predicted values of the specimen's intrinsic fracture toughness (K_{IC}^{In}), the path contribution of the fracture toughness (K_{IC}^{Path}) [18], and the overall fracture toughness (K_{IC}^{Pre}) can be calculated:

$$K_{IC}^{In}=K_{IC} \tag{13}$$

$$K_{IC}^{Path}=K_{IC}(\sqrt{R}-1) \tag{14}$$

$$K_{IC}^{Pre}=K_{IC}^{In}+K_{IC}^{Path}=K_{IC}\sqrt{R} \tag{15}$$

Figure 7 displays the tensile curves for various samples at 650 °C, indicating an average elastic modulus of 23 GPa at this temperature. Subsequently, the area under the stress−strain curve from 0 to ε_u, representing the specific energy of deformation A_v, can be calculated using Origin Pro software. The predicted values of the inherent fracture toughness (K_{IC}^{In}), path contribution of fracture toughness (K_{IC}^{Path}), and overall fracture toughness (K_{IC}^{Pre}) of different samples can be obtained by substituting the values of the elastic modulus and deformation specific energy into Eqs. (12), (14), and (15). The calculated results are listed in Table 4, and the experimentally obtained fracture toughness values (K_{IC}^{Exp}) are listed and compared. This comparative analysis helps in understanding the impact of both intrinsic and extrinsic factors on the fracture toughness of the material studied.

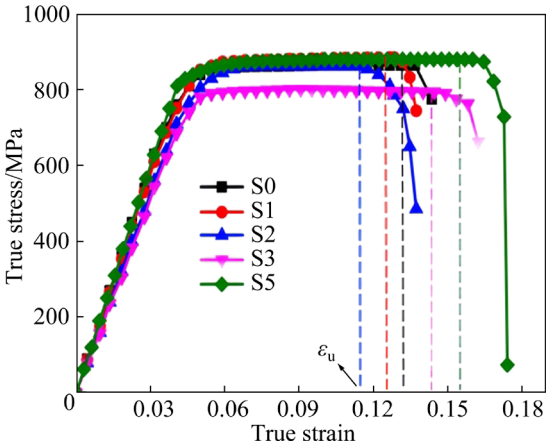

Fig. 7 Stress−strain curves of different specimens under tension at 650 °C

The prediction model accurately forecasts the fracture toughness of samples with varying microstructures. The maximum deviation observed is merely 8.6%. Firstly, there is a clear correlation between the inherent fracture toughness of various samples and the $B2$ phase content. It is demonstrated that a higher $B2$ phase content correlates with increased inherent fracture toughness, which is attributed to the significant contribution of $B2$ phase to plastic deformation. Secondly, the path contribution to fracture toughness, K_{IC}^{Path}, depends on the morphology and distribution of the $\alpha 2$ and O phases. Notably, Sample S2 possesses the highest K_{IC}^{Path} value (14.9 MPa·m$^{1/2}$), attributable to the prevalence of cluster structures within it. As analyzed in Section 3.3, the cluster structure markedly influences the propagation path of the main crack, substantially altering its trajectory.

Table 4 Comparison between experimental values and calculation results of prediction model

Sample	A_v	K_{IC}^{Exp}/(MPa·m$^{1/2}$)	K_{IC}^{Pre}/(MPa·m$^{1/2}$)	Error/%	K_{IC}^{In}/(MPa·m$^{1/2}$)	K_{IC}^{Path}/(MPa·m$^{1/2}$)
S0	98.5	55.1	60.3	8.6	53.5	6.8
S1	92.3	61.9	57.0	8.5	51.8	5.18
S2	75.6	62.2	61.8	0.65	46.9	14.9
S3	76.3	68.4	63.5	7.7	52.9	10.6
S5	120.7	78.0	73.0	6.8	59.2	13.8

The K_{IC}^{Path} value for Sample S0 is only 6.8 MPa·m$^{1/2}$, due to the abundance of acicular *O* phases within it, which hinders the enhancement of crack path tortuosity. The critical K_{IC}^{Path} value for Sample S1 stands at 7.5 MPa·m$^{1/2}$, stemming from a greater proportion of equiaxed *α*2 phase. This promotes the nucleation and propagation of numerous microcracks at the interface between equiaxed *α*2 and *B*2 phases during plastic deformation. These microcracks merge with the primary crack during propagation, thereby considerably shortening its path and impacting overall fracture toughness.

4 Conclusions

(1) Various microstructures of the Ti−22Al−26Nb alloy are achieved through different hot-compression and solution-aging treatments. At high temperatures, the fracture toughness of Ti−22Al−26Nb alloy shows variability corresponding to its microstructure. A peak fracture toughness of 78 MPa·m$^{1/2}$, representing 41.7% increase over the original sample, is attained at a deformation temperature of 1020 °C with 60% deformation amount.

(2) The toughening mechanism of the Ti−22Al−26Nb alloy at 650 °C is sensitive to the content and morphology of the constituent phases. An increased *B*2 phase content results in elevated intrinsic fracture toughness. The Widmanstätten structures yield a markedly tortuous fracture path, while lath at the grain boundary causes the crack propagation path to deflect perpendicularly.

(3) The crack propagation mechanism in the cluster structure of the Ti−22Al−26Nb alloy is influenced by the angle between the crack and the *O*-phase lath. A vertical angle induces both translaminar and interlaminar fractures, an acute angle precipitates translaminar fracture, and an angle near 0° permits crack bridging, thereby enhancing the toughness.

(4) Based on the Griffith−Orowan−Irwin relation and accounting for both the inherent and path contributions to fracture, a predictive model for the fracture toughness of Ti−22Al−26Nb alloy is established. The predicted values of the inherent fracture toughness (K_{IC}^{In}), path contribution of fracture toughness (K_{IC}^{Path}), and overall fracture toughness (K_{IC}^{Pre}) of the Ti−22Al−26Nb alloy with different structures can be obtained, with a prediction error less than 8.6%.

CRediT authorship contribution statement

Yong-qiang ZHANG: Investigation, Validation, Writing – Original draft; **Ke-min XUE:** Validation; **Miao MENG:** Writing – Review & editing; **Si-liang YAN:** Software, Data curation; **Ping LI:** Funding acquisition, Methodology, Resources.

Declaration of competing interest

The authors declare that they have no known competing financial interests or personal relationships that could have appeared to influence the work reported in this paper.

Acknowledgments

This work was financially supported by the National Natural Science Foundation of China (Nos. 51975175, 51875158).

References

[1] BANERJEE D. The intermetallic Ti_2AlNb: Progress in materials science [J]. Progress in Materials Science, 1997, 42: 135−158.

[2] BOEHLERT C J, MAJUMDAR B S, SEETHARAMAN V, MIRACLE D B. The microstructural evolution in Ti−Al−Nb *O*+Bcc orthorhombic alloys [J]. Metallurgical and Materials Transactions A, 1999, 30: 2305−2323.

[3] COWEN C J, BOEHLERT C J. Microstructure, creep, and tensile behavior of a Ti−21Al−29Nb(at.%) orthorhombic+*B*2 alloy [J]. Intermetallics, 2006, 14: 412−422.

[4] LI Shi-qing, MAO Yong, ZHANG Jian-wei, LI Jun-tao, CHENG Yun-jun, ZHONG Zeng-yong. Effect of microstructure on tensile properties and fracture behavior of intermetallic Ti_2AlNb alloys [J]. Transactions of Nonferrous Metals Society of China, 2002, 12: 582−586.

[5] ZHANG Hong-yu, LI Chong, MA Zong-qing, HUANG Yuan, YU Li-ming, LIU Yong-chang. Static coarsening behavior of a pre-deformed Ti_2AlNb-based alloy during heat treatment [J]. Vacuum, 2019, 169: 108934.

[6] ZHANG Ji-kui, CHENG Xiao-quan, LI Zheng-neng. Total fatigue life prediction for Ti-alloys airframe structure based on durability and damage-tolerant design concept [J]. Materials & Design, 2010, 31: 4329−4335.

[7] NAHM S H, SUH C M, JUNG M W, KIM J Y, YANG C H. Application of damage tolerance approach for turbine disk life extension [J]. International Journal of Modern Physics B, 2003, 17: 1916−1921.

[8] ZHAO Yong-qiang, QU Heng-lei. Research on high strength and high toughness titanium alloy with damage tolerance [J].

Materials Science Forum, 2010, 654/655/656: 586−589.

[9] GOGIA A K. High-temperature titanium alloys [J]. Defence Science Journal, 2005, 55: 149−173.

[10] HOMAM N M. Microstructural investigation and castability anticipation in modern Ti/Al/Nb-containing nickel-based superalloys [J]. Transactions of Nonferrous Metals Society of China, 2016, 26: 1607−1619.

[11] FU Yan-qi, LV Man-qian, ZHAO Qing, ZHANG Hai-ming, CUI Zhen-shan. Investigation on the size and distribution effects of *O* phase on fracture properties of Ti_2AlNb superalloy by using image-based crystal plasticity modeling [J]. Materials Science and Engineering A, 2021, 805: 140787.

[12] ZHANG Qin-chai, CHEN Ming-he, WANG Hui, WANG Ning, OUYANG Jin-dong, LIX in-xiao. Thermal deformation behavior and mechanism of intermetallic alloy Ti_2AlNb [J]. Transactions of Nonferrous Metals Society of China, 2016, 26: 722−728.

[13] WITTKOWSKY B, PFUFF M, DOGAN B, SCHWALBE K H, WAGNER R. Statistical treatment of fracture toughness data of Ti−A1−Si−Nb alloys [J]. Materials Science and Engineering A, 1994, 187: 105−111.

[14] LIU Tian-yu, MIN Xiao-hua, ZHANG Shuang, WANG Cun-shan, DONG Chuang. Microstructures and mechanical properties of Ti−Al−V−Nb alloys with cluster formula manufactured by laser additive manufacturing [J]. Transactions of Nonferrous Metals Society of China, 2021, 31: 3012−3023.

[15] ZHANG Shun-ke, TIAN Ning, LI De-yuan, LI Jiang-hua, JIN Fang-wei, WANG Guang-yan, TIAN Su-gui, Microstructure evolution and fracture mechanism of a TiAl−Nb alloy during high-temperature tensile testing [J]. Materials Science and Engineering A, 2022, 831: 142094.

[16] YUE Xiao-an, SHEN Jun, XIONG Yi-long, LI Qiu-dong, ZHENG Shao-kai. Microstructure, fracture toughness and high-temperature tensile property of large size Ti−46Al−5Nb−0.18C−0.3Si alloy with oriented lamella by electromagnetic confinement directional solidification [J]. Materials Science and Engineering A, 2021, 812: 141139.

[17] WANG Yong-zhe, DING Hong-sheng, ZHANG Hai-long, CHEN Rui-run, GUO Jing-jie, FU Heng-zhi. Microstructures and fracture toughness of Ti−(43−48)Al−2Cr−2Nb prepared by electromagnetic cold crucible directional solidification [J]. Materials & Design, 2014, 64: 153−159.

[18] SHI Xiao-hui, ZENG Wei-dong, SHI Chun-ling, WANG Hao-jun, JIA Zhi-qiang. The fracture toughness and its prediction model for Ti−5Al−5Mo−5V−1Cr−1Fe titanium alloy with basket-weave microstructure [J]. Journal of Alloys and Compounds, 2015, 632: 748−755.

[19] FAN J K, LI J S, KOU H C, HUA K, TANG B. The interrelationship of fracture toughness and microstructure in a new near β titanium alloy Ti−7Mo−3Nb−3Cr−3Al [J]. Materials Characterization, 2014, 96: 93−99.

[20] ZHENG You-ping, ZENG Wei-dong, LI Dong, MA Hao-yuan, ZHANG Peng-hui, MA Xiong. Quasi cleavage fracture of the bimodal size lamellar O phase microstructure of a Ti2AlNb based alloy [J]. Journal of Alloys and Compounds, 2019, 799: 267−278.

[21] LIU Xiao-yu, XIONG Zhi-hua, ZHANG Hui-mei. Nonlinear strain energy based (NSEB) criterion for quasi-brittle materials under multiaxial stress states [J]. Construction and Building Materials, 2023, 375: 131001.

[22] CHO L, BRADLEY P E, LAURIA D S, MARTIN M L, CONNOLLY M J, BENZING J T, SEO E J, FINDLEY K O, SPEER J G, SLIFKA A J. Characteristics and mechanisms of hydrogen-induced quasi-cleavage fracture of lath martensitic steel [J]. Acta Materialia, 2021, 206: 116635.

[23] PARADKAR A, KUMAR V, KAMAT S V, GOGIA A K, KASHYAP B P. The effect of grain size and composition on the fracture toughness of Ti−Al−Nb alloys undergoing stress-induced martensitic transformation [J]. Materials Science and Engineering A, 2008, 486: 273−282.

[24] SHAO Bin, SHAN De-bin, GUO Bin, ZONG Ying-ying. Plastic deformation mechanism and interaction of *B*2, α2, and *O* phases in Ti−22Al−25Nb alloy at room temperature [J]. International Journal of Plasticity, 2019, 113: 18−34.

[25] ANTONOV R. Method of accelerated fracture toughness K_{IC} testing of metallic materials [J]. Strength of Materials, 1984: 179−184.

[26] MAKHUTOV N A. Griffith theory and development of fracture mechanics criteria [J]. Materials Science and Engineering A, 1993: 316−319.

[27] ZHONG Qun-peng, ZHAO Zi-hua. Fractography [M]. Beijing: Higher Education Press, 2006: 30−33. (in Chinese)

[28] ZHANG Peng-hui, ZENG Wei-dong, ZHENG You-ping, XU Jian-wei, LIANG Xiao-bo, ZHAO Yong-qing. Fracture toughness of Ti−22Al−25Nb alloy at room and high temperatures [J]. Materials Science and Engineering A, 2020, 796: 140009.

[29] ZHENG You-ping, ZENG Wei-dong, LI Dong, ZHAO Qing-yang, LIANG Xiao-bo, ZHANG Jian-wei, MA Xiong. Fracture toughness of the bimodal size lamellar *O* phase microstructures in Ti−22Al−25Nb (at.%) orthorhombic alloy [J]. Journal of Alloys and Compounds, 2017, 709: 511−518.

[30] ARATA J J M, KUMAR K S, CURTIN W A, NEEDLEMAN A. Crack growth in lamellar titanium aluminide [J]. International Journal of Fracture, 2001, 111: 163−189.

[31] CHEN Yu-yong, NIU Hong-zhi, KONG Fan-tao, XIAO Shu-long. Microstructure and fracture toughness of a β phase containing TiAl alloy [J]. Intermetallics, 2011, 19: 1405−1410.

[32] XU Xue-song, DING Hong-sheng, LI Wei, HUANG Hai-tao, LIANG He, SEUNGMI K, CHEN Rui-run, GUO Jing-jie, FU Heng-zhi. The smooth and notched three-point bending fatigue behavior of directionally solidified high-Nb TiAl alloy [J]. Materials Characterization, 2021, 181: 111444.

具有不同典型显微组织 Ti−22Al−26Nb 合金的高温断裂行为

张勇强，薛克敏，孟 淼，严思梁，李 萍

合肥工业大学 材料与科学工程学院，合肥 230009

摘 要：研究了具有双峰板条组织、双态组织和魏氏组织的 Ti−22Al−26Nb 合金的高温断裂行为。通过跨相区压缩变形和随后的热处理制备合金样品。结果表明，与具有初始微观结构的合金相比，Ti−22Al−26Nb 合金在 650 ℃下的断裂韧性增加了 41.7%。*B*2 相的含量决定材料的固有断裂韧性，而析出相的形态和分布影响裂纹扩展路径的曲折性。在微观结构中，层片的形态和几何方向对裂纹路径有最大影响，Widmanstätten 结构表现出最曲折的断裂路径。此外，开发了一种断裂韧性预测模型；该模型能准确预测具有不同显微组织的 Ti−22Al−26Nb 合金在 650 ℃的断裂韧性。

关键词：Ti_2AlNb 基合金；典型显微组织；断裂韧性预测模型；断裂力学

(Edited by Bing YANG)